Astroparticle Physics 29 (2008) 453–460

Contents lists available at ScienceDirect

Astroparticle Physics

journal homepage: www.elsevier.com/locate/astropart

The cosmic ray primary composition at the knee region from lateral distributions of atmospheric Čerenkov photons in extensive air showers

H. Tokuno [a,*], F. Kakimoto [a], S. Ogio [a,1], D. Harada [a], Y. Kurashina [a], Y. Tsunesada [a], N. Tajima [b], Y. Matsubara [d], A. Morizawa [c], O. Burgoa [a], E. Gotoh [b], K. Kadota [e], T. Kaneko [f], M. Kubo [c], P. Miranda [g], T. Mizobuchi [c], Y. Mizumoto [h], K. Murakami [d,2], H. Nakatani [b], K. Nishi [b], S. Shimoda [b], Y. Shirasaki [h], Y. Toyoda [i], A. Velarde [g], K. Yamada [a], Y. Yamada [b], H. Yoshii [c]

[a] Department of Physics, Tokyo Institute of Technology, Meguro, Tokyo 152-8551, Japan
[b] RIKEN (The Institute of Physical and Chemical Research), Wako, Saitama 351-0198, Japan
[c] Department of Physics, Ehime University, Matsuyama, Ehime 790-8577, Japan
[d] Solar-Terrestrial Environment Laboratory, Nagoya University, Nagoya, Aichi 464-8601, Japan
[e] Faculty of Engineering, Musashi Institute of Technology, Setagaya, Tokyo 158-8557, Japan
[f] Department of Physics, Okayama University, Okayama, Okayama 700-8530, Japan
[g] Instituto de Investigaciones Fisicas, Universidad Mayor de San Andres, La Paz 8635, Bolivia
[h] National Astronomical Observatory of Japan, Mitaka, Tokyo 181-8588, Japan
[i] Faculty of Science, Kobe University, Kobe, Hyogo 657-8501, Japan

ARTICLE INFO

Article history:
Received 31 January 2008
Received in revised form 15 May 2008
Accepted 19 May 2008
Available online 24 May 2008

PACS:
96.40.−z
96.40.De
96.40.Pq

Keywords:
Cosmic rays
Extensive air showers
Atmospheric Čerenkov
Chemical composition
Knee

ABSTRACT

We have measured the lateral distributions of atmospheric Čerenkov photons associated with extensive air showers to study the chemical composition of the primary cosmic rays in the energy range from $10^{14.5}$ to 10^{16} eV, so called knee region. The atmospheric Čerenkov photon detectors were installed in the EAS array at Mt. Chacaltaya. The measured lateral distributions were fitted with an empirical formula with a parameter which is sensitive to mass numbers of primary cosmic rays. A three species model (proton, carbon, and iron nuclei) is used for the chemical composition study of the present experiment. To determine the mixing ratio of the three species, the distributions of the parameter for the observed events were examined to reproduce those for the simulated ones calculated with the CORSIKA code using the QGSJET hadronic interaction model. From the obtained mixing ratio of the three species, we determined the mean logarithmic mass numbers of primary cosmic rays, $\langle \ln A \rangle$, in the knee region. The present result shows that the values of $\langle \ln A \rangle$ are higher than the logarithmic mass number for carbon and the proton component is no more dominant at the knee.

1. Introduction

The energy spectrum of cosmic rays is expressed by power law in the wide energy range from 10^{10} to 10^{20} eV. A number of detailed studies on the fine structure of the spectrum revealed that the power law index changes from −2.7 to −3.0 around $10^{15.5}$ eV (e.g. [1]). In particular, in this energy region known as the "knee", some experimental results have suggested that the cosmic ray primary composition also changes with increasing energies (e.g. [1]). These changes at the knee are of special interest in cosmic ray physics, because they must be related to the origin of the cosmic rays, and to both acceleration mechanisms at the sites and propagation mechanisms in the Galaxy (e.g. [2–5]). Further investigation of the chemical composition of the primary cosmic rays into details is required to solve those problems. In the energy region below the knee, primary cosmic rays are detected directly with balloon-borne and satellite equipments (e.g. [6,7]). On the direct measurements charges of the primary cosmic rays are determined through ionization losses in the detectors, and these types of detectors have the ability to discriminate primary cosmic rays among several groups.

* Corresponding author. Present address: Institute for Cosmic Ray Research, University of Tokyo, Kashiwa, Chiba 277-8582, Japan. Tel.: +81 4 7136 5153; fax: +81 4 7136 3134.
E-mail address: htokuno@icrr.u-tokyo.ac.jp (H. Tokuno).
[1] Present address: Department of Physics, Osaka City University, Sumiyoshi, Osaka 558-8585, Japan.
[2] Deceased.

0927-6505/$ - see front matter © 2008 Elsevier B.V. All rights reserved.
doi:10.1016/j.astropartphys.2008.05.001

Therefore with these measurements one can obtain component spectra for several mass groups of species. According to these measurements, it is obvious that the dominant component below 10^{14} eV is protons. On the other hand, in the energy region at and above the knee it is difficult to measure the spectra of the primary particles by such direct measurements because of their low intensities and limited aperture of the detectors. Therefore, the chemical composition in this energy region is determined through the measurement of extensive air shower (EAS).

The BASJE group had carried out EAS experiments of two independent measurements to study the chemical composition, and we have reported the results of the mean logarithmic mass number of primary cosmic rays $\langle \ln A \rangle$. First, we observed atmospheric Čerenkov photons simultaneously with EASs and determined the chemical composition through analysis of time structures of Čerenkov photon pulses [8]. Second, we investigated the chemical composition through the equi-intensity analysis of the measured EAS size spectra of different incident directions [1]. The time structures of atmospheric Čerenkov photon pulses are good indicators of the longitudinal developments of EASs at their early stages, i.e. above the observation site: since they strongly depend on the primary species, it is possible to investigate the chemical composition. On the other hand, the equi-intensity method is useful to evaluate the longitudinal developments "below" the observer's altitude. At the altitude of Mt. Chacaltaya in Bolivia (5200 m a.s.l., atmospheric depth of 550 g cm^{-2}), the maximum development points of EASs are clearly seen in the equi-intensity curves of the EASs initiated by primary protons with energies above 10^{15} eV. Thus we can examine the chemical composition from the observations of the longitudinal developments above and below their maximum points. Both of these results show that $\langle \ln A \rangle$ increases with energies at the knee [1,8]. Most of other experimental results also have the same tendency: $\langle \ln A \rangle$ above the knee is increasing with energies (e.g. [1,8–11]). However these results of absolute values of $\langle \ln A \rangle$ are different from others around the knee. In order to reduce the systematic uncertainties and to determine the chemical composition in good accuracies, we consider the following requirements: (1) Measure EASs near maximum development points which have less affect of EAS fluctuations. (2) Use an unbiased trigger threshold for heavy components of primaries, of which EAS developments are faster than those of light components at a same energy. (3) Measure the electro-magnetic components which are less dependent on hadronic interaction model than the muon component in EASs. (4) Require a separation capability between the three species (proton, carbon, and iron nuclei). (5) Measure the chemical composition with wide energy range (from direct measurement region to above the knee). The high altitude of our site meets the (1–2) requirements. For the (3–5) requirements, we have measured lateral density distributions of atmospheric Čerenkov photons associated with EASs. Our MC studies showed that the distributions of atmospheric Čerenkov photons of EASs contain integrated information of EAS developments from the first interaction points to the altitude of the observation site, and thus good probe for a chemical composition study. The MC studies also showed that this analysis has a separation capability between the three species below and above the knee, and we can detect sufficient photons per event because Čerenkov photons emitted by EASs arrived at the ground with suffering little attenuation by the air.

We performed the experiment from August 2001 to October 2002 and we collected more than 3000 atmospheric Čerenkov photons events associated with EASs. The lateral distributions of the Čerenkov photons are fitted to an empirical formula with the parameters as primary particle estimators obtained from our Monte-Carlo (MC) studies. We used the three component model (proton, carbon, and iron nuclei), and determined the mixing ratio of these species in primary cosmic rays by comparing the parameter distributions obtained from both of the experiment and the simulated showers. We also calculated the mean logarithmic mass, $\langle \ln A \rangle$.

2. Experiment

The atmospheric Čerenkov photon detectors were installed in the EAS array called the minimum air shower (MAS) array [1] at Mt. Chacaltaya to measure the lateral photon density distributions to study the chemical composition of primary cosmic rays.

2.1. The MAS array

The MAS array consists of 69 scintillation detectors. The arrangement of the array is shown in Fig. 1. The particle detectors measure both or either of the local particle densities and the arrival timings. Using the data obtained with the array we determined the EAS parameters, i.e., arrival directions, core positions, and air shower size N_e. The data acquisition system of the MAS array is triggered by a fourfold coincidence of the fast timing signals with amplitudes greater than 0.8 particle level within 4 μs time window. In order to obtain EAS events efficiently in a wide energy range, the observations were carried out in two modes, the low energy mode (10^{14}–10^{15} eV) and the high energy mode (10^{15}–10^{16} eV), by changing the triggering detectors as shown in Fig. 1. The trigger efficiencies are 100% in both of the observation modes. A further description about the hardware of the array and the details of the analysis procedures are described in previously published papers (e.g. [1,12]).

The determination accuracies for the EAS parameters depend on species of primary particles and their primary energies. We evaluated the accuracies in determination of the EAS parameters (sizes, arrival directions) with MC simulations. The CORSIKA code [13] version 5.61 was employed with the QGSJET hadronic interaction model [14] for the three primary types, proton, carbon, and iron nuclei. The simulated events were reconstructed using the same analysis program to be used in the analysis of the observed data. Fig. 2 shows the simulation results for EASs of incident zenith an-

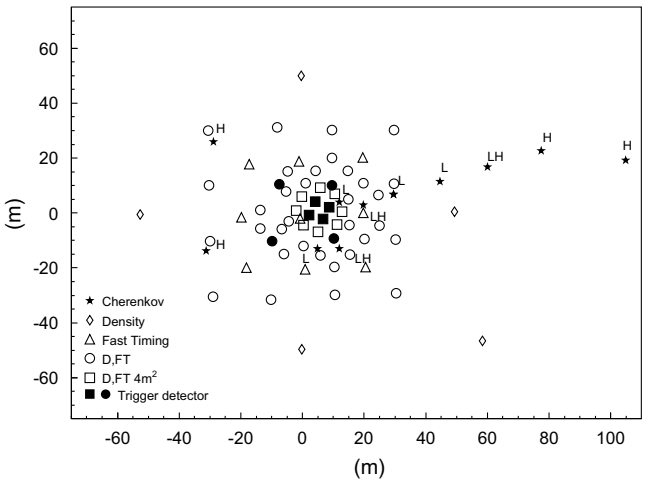

Fig. 1. Layout of the MAS array detectors and atmospheric Čerenkov photon detectors. The array consists of 1 m^2 particle density detectors (diamond), 1 m^2 fast timing (FT) detectors (triangle), 1 m^2 density and FT detectors (open circle), 4 m^2 density and FT detectors (open square). Filled squares are 4 m^2 density and FT detectors used as the trigger detectors in the low energy mode, and filled circles are 1 m^2 density and FT detectors used as those in the high energy mode. Asterisks labeled "L" are the atmospheric Čerenkov detectors used in low energy mode, asterisks labeled "H" are those in the high energy mode.

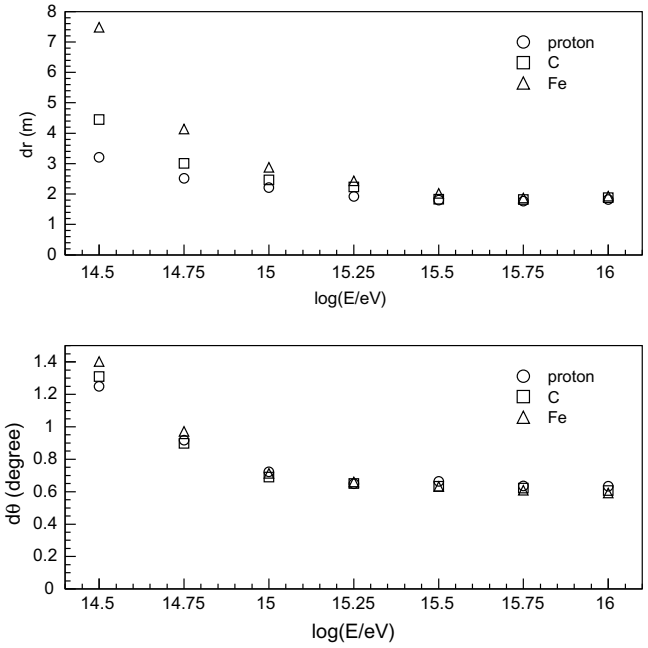

Fig. 2. The measurement errors of 90% C.L. with the MAS array. Upper panel shows the determination accuracy of EAS core positions. Lower panel shows the determination accuracy of arrival directions.

gles less than 30° and core locations within 20 m (for energies $<10^{15}$ eV) and 30 m (for energies $>10^{15}$ eV) from the array center. This figure shows that the accuracy in determination of core positions is 2 m for every species with energies above 10^{15} eV, whereas the arrival directions are determined within the accuracy of 1°. Fig. 3 displays reconstructed N_e as a function of the primary energies for each species. Systematic differences in $\log N_e$, ($\Delta \log N_e$), among the species are shown. For example, $\Delta \log N_e$ between proton and iron nuclei is 0.3 at primary energy of $10^{14.5}$ eV and it is less than 0.2 above $10^{15.0}$ eV. We used those $\Delta \log N_e$ as N_e bin sizes in our analysis. Fig. 4 represents the determination accuracy of N_e

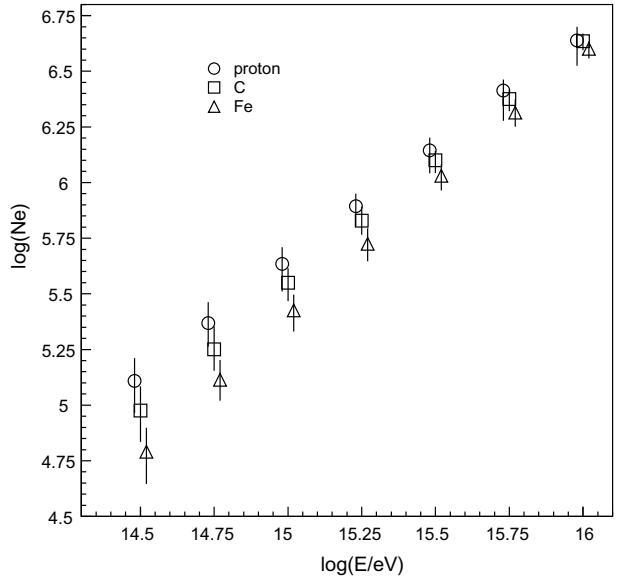

Fig. 3. This panel is the simulated relations between EAS sizes obtained with the air shower analysis and primary energies, for each primary species. The error bars represent 1σ in this figure.

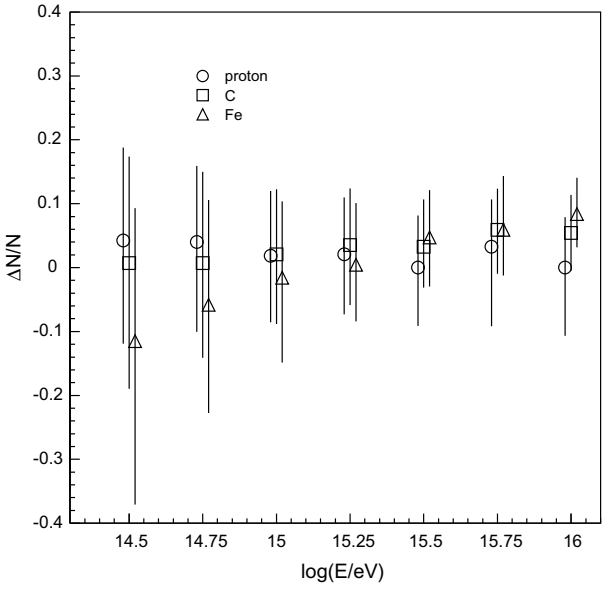

Fig. 4. This panel is the systematic and statistic errors on the size determinations. The error bars represent 1σ in this figure.

as a function of a primary energy for each species, and one can see that the determination errors are smaller than 15%.

2.2. Atmospheric Čerenkov photon detector

To measure lateral density distributions of atmospheric Čerenkov photons, we installed several photon detectors in the MAS array, and these detectors simultaneously operated with the array, i.e., with common data acquisition triggers. Each of the Čerenkov photon detectors installed in the MAS array consists of a 5-inch photo multiplier tube (PMT), HAMAMATSU-R1250. The schematic view of the photon detectors is shown in Fig. 5. Each detector has a field of view of about 1.8 sr. This field of view is determined to obtain atmospheric Čerenkov photons from EASs with their arrival zenith angles of smaller than 30°, since more than 99% of atmospheric Čerenkov photons are concentrated within 15° from the EAS axis. The faceplates of every PMT are covered with a UV filter (Schott-BG3) to reduce the night-sky background (NSB) photons by a factor of about 50%. The output signals of the PMTs are recorded with digital oscilloscopes (Tektronix-TDS303x, TDS3012, Tek2440) with the sampling frequencies of 1 GHz. To achieve a wide dynamic range for the measurements we used two input channels with different vertical ranges for each PMT output. The

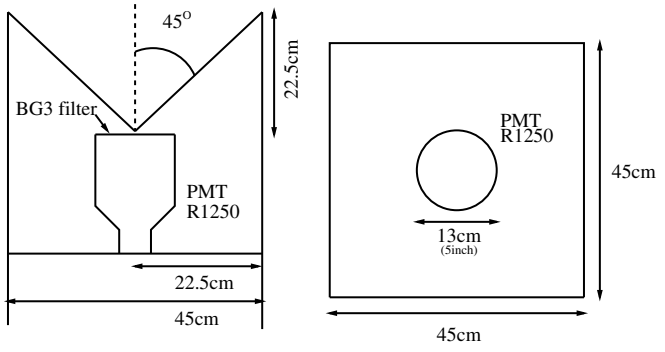

Fig. 5. Left panel is the cross sectional view of one atmospheric Čerenkov photon detector, and right panel is the top view of it.

Table 1
Observation summaries of the Čerenkov experiments

Energy mode	Period (observation time)	Triggered events	DAQ rate (Hz)
L	2001 August 9–October 23 (165 h)	739,347	1.3
H	2002 June 5–October 9 (200 h)	565,864	1.0

The row labeled "L" is the summary of the low energy mode observations, and the row labeled "H" is that of the high energy mode.

maximum voltage for each of the channels is 200 mV and 2 V. The triggering signals of these Čerenkov detectors are generated by the MAS array. The digitized signals on the digital oscilloscopes were stored in the hard disk in a personal computer through the GPIB interface.

The PMT gains are subject to fluctuation mainly caused by variations of temperatures and anode currents. In this experiment, we monitored the relative gain variations within 3 min in every hours during the observations. In the PMT calibrations, a stable radio isotope light pulser is used: $YAlO_3$:Ce scintillator and ^{241}Am (e.g. [15,16]). The typical magnitude of the PMT gain fluctuations was evaluated as smaller than 2% in an observation night. The main source of these fluctuations can be explained in terms of the variations in temperatures. Using the calibration data of the PMT gains, we corrected the numbers of atmospheric Čerenkov photons in the analysis procedure.

2.3. Observation

The experiment was carried out with two observational mode. In the low energy mode observations from August to October 2001, the target primary energy of cosmic rays was from 10^{14} to 10^{15} eV. We installed seven Čerenkov photon detectors in the array at the distances from 10 to 70 m. In the high energy mode observations from June to October 2002, the target energy of cosmic rays was from 10^{15} to 10^{16} eV, and we used eight detectors installed in a wider area to measure the lateral distributions of atmospheric Čerenkov photons within 130 m from the air shower cores. The Čerenkov photon detector configurations are shown in Fig. 1.

The data acquisition rate was limited by the data transfer speed from the oscilloscopes to the PCs through GPIB interface, and the rate is about 1 Hz in each observation mode. The total observation times are about 360 h, and the duty cycle was approximately 8.5%. The number of total triggered events is 1.3×10^6 (Table 1).

3. Atmospheric Čerenkov photon Simulation

Hillas et al. proposed a parametrized formula of the lateral density distribution of atmospheric Čerenkov photons emitted from EASs applicable for sea level experiments [17]. In some experiments at lower altitudes the expression has been adopted in their analyses (e.g. [9]), however, it does not give the best fit for our experiment. Therefore we studied lateral density distributions of atmospheric Čerenkov photons $\rho(r)$ as a function of the shower axis at the altitude of our site. From EAS simulations using the CORSIKA code with the QGSJET hadronic interaction model, we found an empirical formula,

$$\rho(r) = \alpha \cdot \left(\frac{r}{R_0}\right)^{-(\beta + r/R_0)}, \quad (1)$$

where R_0 is a constant determined from the simulation, α is a normalization factor, and β is the fitting parameter. The parameter β in the exponent is a good indicator of the primary species, and the separation power using β depends on choices of the constant, R_0. By our simulation study, we found that $R_0 = 70$–110 m gives more robust results, and systematic uncertainties on $\langle \ln A \rangle$ are smaller than 0.3 in each energy mode. We chose $R_0 = 90$ m to obtain the most efficient separations using the parameter β. Fig. 6 is the plot of an example of the observed data (core distance = 29 m, zenith angle = 29°, and $\log N_e = 6.1$), and the line on this figure is the result of fitting with the formula we employed in this work. In this figure the bars are due to the Poisson fluctuations of the photons at the detectors and the uncertainties in the EAS core determinations.

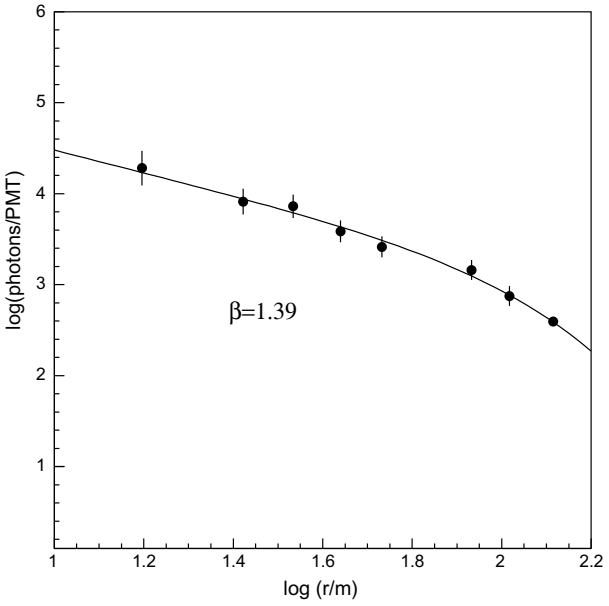

Fig. 6. An observed lateral density distribution of atmospheric Čerenkov photons densities induced by our air shower event and the best curve with function (1). The error bars on this plot shows the statistical error and the determination error of the EAS core position.

To examine the chemical composition as a function of the energy, we obtained the distributions of the parameter β from the simulation studies for each of the three species (proton, carbon, and iron nuclei) in some intervals of the shower sizes. We choose the bin size in N_e from the determination accuracy for EAS N_e mentioned in Section 2.1. The observed EAS events are classified by their sizes N_e, and then the observed β distribution in each N_e bin is compared with the distribution obtained from the simulation. To reduce simulation times, we used the thinning option of the CORSIKA code [18]. From the simulations with various thinning levels, the thinning factor of 10^{-6} and confirmed that it is most effective in reducing the computation times and does not bring obvious systematic errors. In these simulations, we assumed that the differential cosmic ray energy spectrum is of power law with the index of -2.7 below $10^{15.5}$ eV and of -3.2 above this energy (refer to our previous result [1]). In the simulation of the atmospheric Čerenkov photon emission, we used the US standard atmosphere model and considered the Rayleigh and the Mie scatterings. We also considered the contamination of the signals by the NSBs using the atmospheric monitoring data. To reproduce the waveform from the simulated/observed data, we took account of the system responses including the detector configurations and the signal attenuation in the cables.

4. Analysis

We employed a data cut to select well determined EAS events with the criteria listed in the Table 2. The number of the selected events was 3100. Furthermore, these events were selected in the analysis of the Čerenkov photons with the following criteria; the

Table 2
The event selection criteria of air shower sizes and core locations, and the numbers of the remained events

$\log N_e$	Core distance (m)	Number of events
5.0–5.3 (L)	<10	327
5.3–5.6 (L)	<20	383
5.5–5.7 (H)	<30	1260
5.7–5.9 (H)	<30	626
5.9–6.1 (H)	<30	293
6.1–6.3 (H)	<30	130
6.3–6.5 (H)	<30	74

The label "(L)" indicates a condition for the low energy mode observations, and the label "(H)" indicates that for the high energy mode.

reduced χ^2 of the fitting to the lateral density distribution function is smaller than 4; the number of hit detectors with output pulses with amplitudes larger than 9σ above the NSB is greater than 4. With this hit condition more than 99% of accidental hits by fluctuations of NSB are eliminated. We confirmed that there are no selection bias for every species by these criteria described above. After these data cuts, 3093 events remained (Table 2). To determine the mixing ratio of the three species x_i ($\sum x_i = 1$, i = proton, carbon, and iron nuclei), we employed a method based on the maximum likelihood technique. We calculated the probability distribution function (PDF) of the parameter β, $p_i(\beta)$, from the simulation studies for each of the shower size bins. Once the PDFs of β are known, we can evaluate an expected distribution of β for a given mixing ratio $\mathbf{x}$

$$P(\beta;\mathbf{x}) \equiv \sum_i x_i p_i(\beta). \tag{2}$$

The problem we tackle is to find the mixing ratio $\mathbf{x}_{\max}$ to reproduce the observed distribution of β, as $p(\beta^{\text{obs}}) = P(\beta;\mathbf{x}_{\max})$. The maximum likelihood method tells us that the best estimate of $\mathbf{x}$ is such that maximizes the likelihood function defined as

$$L(\mathbf{x}) = \prod_{j=1}^{N} P(\beta_j^{\text{obs}};\mathbf{x}), \tag{3}$$

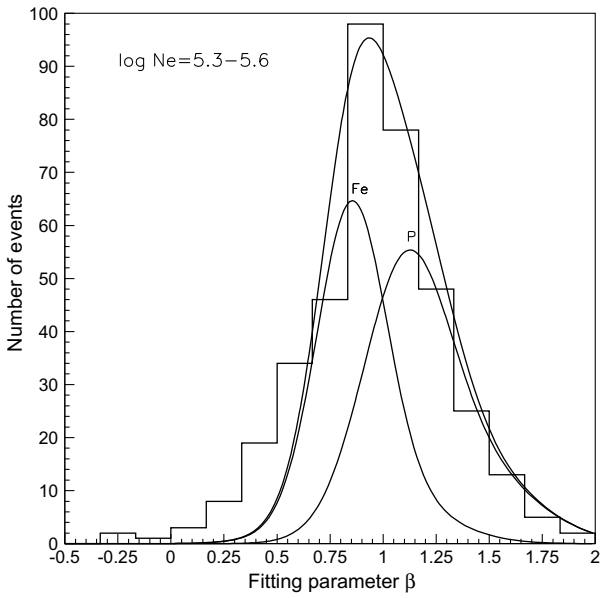

Fig. 8. The distributions of the fitting parameter β for the observed events and those simulated in the size bin of $\log N_e$ = 5.3–5.6.

where N is the number of events in the shower size bin of interest. We showed the distributions of the observed parameter β_j^{obs} in Figs. 7–13. From these observed β_j^{obs} we obtained the maximum likelihood ratio of the three primary nucleus types, for example $\mathbf{x}_{\max}$ ($\log N_e$ = 5.5–5.7) = (0.22, 0.45, 0.33) (Table 3). The simulated PDFs of β for the three species with the mixing ratio of $\mathbf{x}_{\max}$ ($\log N_e$ = 5.5–5.7) obtained from the maximum likelihood method are superimposed on the histogram of β for observed events in Fig. 9.

The 90% confidence intervals of $\mathbf{x}_{\max}$ were evaluated by a likelihood ratio test. First, we obtained a PDF of β from the simulated events of the same number of the observed events with obtained $\mathbf{x}_{\max}$. Second, the mixing ratio of the three species $\mathbf{x}_{\text{est}}$ was estimated using the previous maximum likelihood method. The estimated mixing ratio $\mathbf{x}_{\text{est}}$ could differ from the $\mathbf{x}_{\max}$ by the

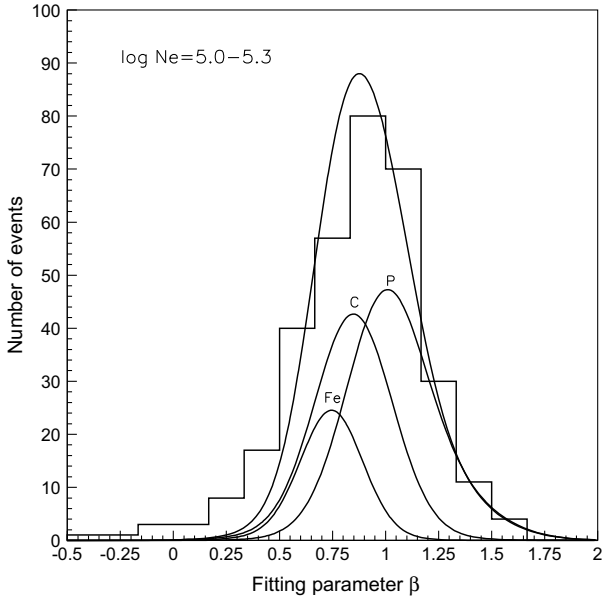

Fig. 7. The distributions of the fitting parameter β for the observed events and those simulated in the size bin of $\log N_e$ = 5.0–5.3.

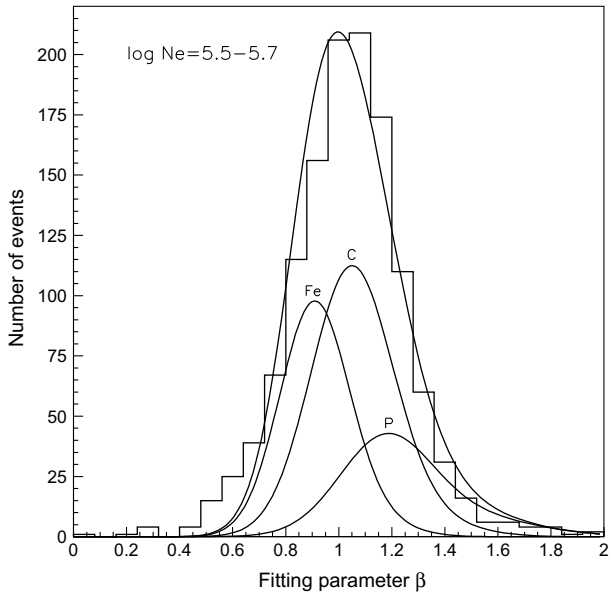

Fig. 9. The distributions of the fitting parameter β for the observed events and those simulated in the size bin of $\log N_e$ = 5.5–5.7.

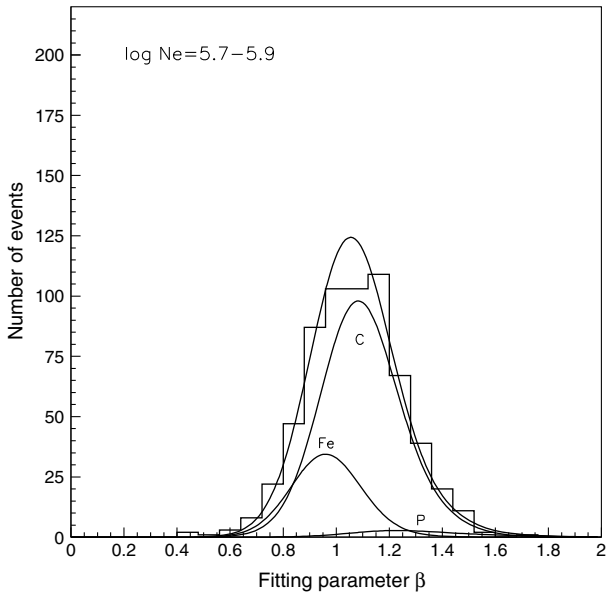

Fig. 10. The distributions of the fitting parameter β for the observed events and those simulated in the size bin of $\log N_e = 5.7$–5.9.

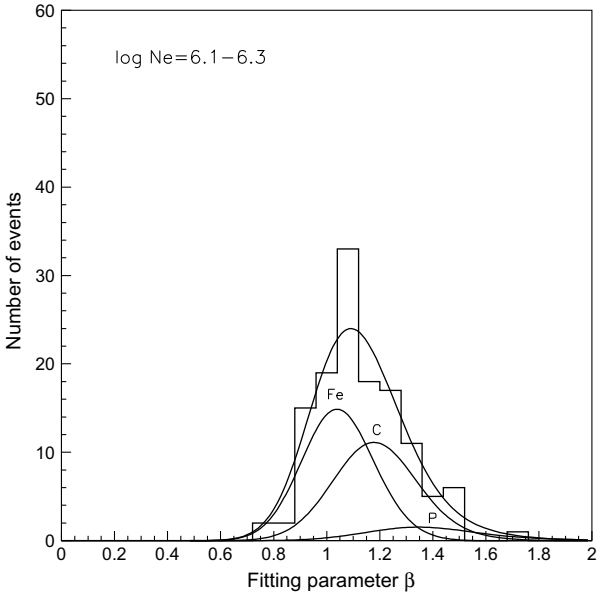

Fig. 12. The distributions of the fitting parameter β for the observed events and those simulated in the size bin of $\log N_e = 6.1$–6.3.

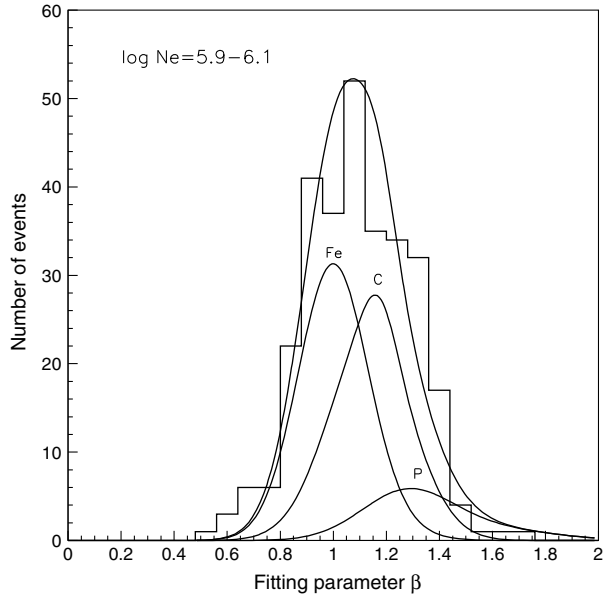

Fig. 11. The distributions of the fitting parameter β for the observed events and those simulated in the size bin of $\log N_e = 5.9$–6.1.

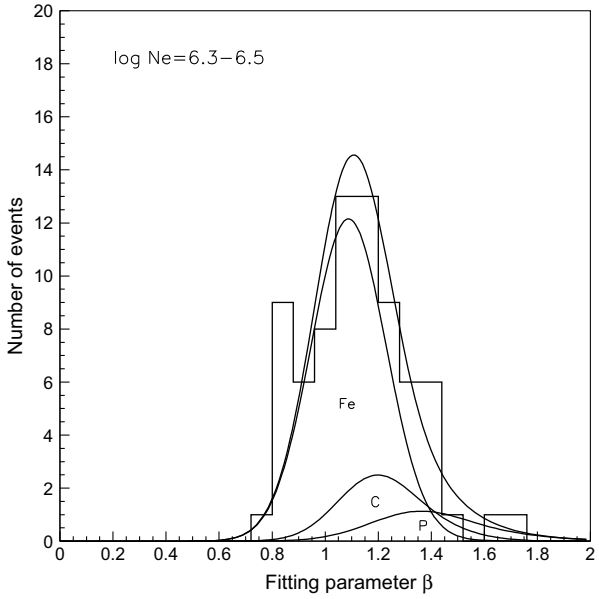

Fig. 13. The distributions of the fitting parameter β for the observed events and those simulated in the size bin of $\log N_e = 6.3$–6.5.

separation capability. Third, we determined a log-likelihood ratio statistic

$$\kappa = \ln \frac{L(\mathbf{x}_{\max})}{L(\mathbf{x}_{\text{est}})}. \quad (4)$$

To obtain the κ distribution, these procedure are contained with 1000 times for each N_e size bin. From the κ distribution, we obtain the "critical limit" of κ_{90} ($\kappa < \kappa_{90}$ appears with the 90% probability). The group of $\mathbf{x}$ with $\kappa < \kappa_{90}$ includes $\mathbf{x}_{\max}$ within 90% confidence level, and indicates the 90% confidence level of the mixing ratio for each of the three species. To calculate $\langle \ln A \rangle$, we assume that the indices of energy spectrum of the three species is constant in an energy bin, and use the power law spectrum index of all particle spec-

Table 3
The measured mixing ratio of three species, $\mathbf{x} = (x_{\text{proton}}, x_C, x_{Fe})$ in each size bin

$\log N_e$	x_{proton} (%)	x_C (%)	x_{Fe} (%)
5.0–5.3 (L)	46^{+15}_{-15}	37^{+31}_{-33}	17^{+21}_{-16}
5.3–5.6 (L)	54^{+17}_{-20}	0^{+33}	46^{+16}_{-21}
5.5–5.7 (H)	22^{+7}_{-6}	45^{+10}_{-12}	33^{+10}_{-6}
5.7–5.9 (H)	3^{+6}_{-3}	74^{+11}_{-12}	23^{+9}_{-9}
5.9–6.1 (H)	13^{+11}_{-13}	42^{+18}_{-38}	45^{+13}_{-25}
6.1–6.3 (H)	8^{+14}_{-7}	43^{+27}_{-29}	49^{+22}_{-23}
6.3–6.5 (H)	10^{+19}_{-10}	17^{+34}_{-17}	73^{+20}_{-46}

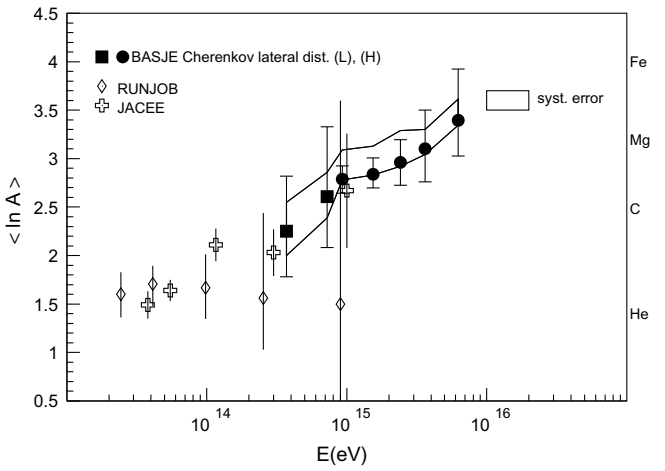

Fig. 14. Mean logarithmic mass $\langle \ln A \rangle$ obtained with the present experiment as a function of energy, the error bars and the error box represent the 90% C.L. statistic errors and the systematic error, respectively. The plots in energies represent a weighted mean of the median energy of the every species in an energy bin. For comparison, direct measurements results (JACEE [6] and RUNJOB 2001 [7]) are also shown.

trum to our previous result [1]. The mixing ratio of the three species in the energy range $E \sim E + dE$ is calculated as

$$x_i = \frac{x_i' \int F_i(E, N_e, dN_e) E^{-\gamma} dE}{\sum x_i' \int F_i(E, N_e, dN_e) E^{-\gamma} dE}, \quad (5)$$

where $F_i(E, N_e, dN_e)$ is the PDF of energy E for showers reconstructed in the size range $N_e \sim N_e + dN_e$, x_i' is a constant in the energy bin. The all particle spectrum is expressed as $E^{-\gamma}$. For all of the three species the index of differential energy spectrum γ was adopted -2.7 below $10^{15.5}$ eV and -3.2 above. The confidence intervals of $\mathbf{x}'$ with the 90% confidence level were estimated by the likelihood ratio test described above. Fig. 14 shows the obtained $\langle \ln A \rangle$ as a function of energy.

We evaluated systematic errors of these results. First, we consider the systematic errors due to the assumption of the cosmic ray all particle spectrum and the knee energy on the basis of our previous observations. Since the spectral index and the position of the knee used in this work contain errors as $\Delta\gamma = \pm 0.1$ and $\Delta \log E_{\mathrm{knee}} = \pm 0.1$, respectively, we calculated the systematic effects on $\langle \ln A \rangle$ with MC simulations. We found that the differences on $\langle \ln A \rangle$ are smaller than 0.03 at $10^{14.5}$ eV and smaller than 0.01 at 10^{16} eV. We conclude that the systematic error due to the assumption on the spectrum is negligibly small compared to the statistical errors shown in Fig. 14.

The other systematic error is attributed to the three species model used in this analysis. We evaluated the determination accuracy for $\langle \ln A \rangle$ by three species model for the three species themselves and their middle components; we are concerned here with helium and magnesium. From the simulation studies, determination accuracy for $\langle \ln A \rangle$ for each species (the three species, and middle components: helium and magnesium) are obtained, and shown in Table 4. In the each bin the largest systematic differences of them are employed as the systematic errors and are shown in Fig. 14. These systematic errors are less than 0.3 on $\langle \ln A \rangle$.

From the above analyses, we obtained the following result. The values of $\langle \ln A \rangle$ are higher than the logarithmic mass number for carbon ($\ln A = 2.49$) at the knee, as shown in Fig. 14. This result is not affected by the systematic error from the determination accuracy for $\langle \ln A \rangle$. The best-fit rate of $d\langle \ln A \rangle / d\log E$ for the whole energy range is 0.65 ± 0.4 with $\chi^2 = 0.44$. A constant composition model gives a fit of $\langle \ln A \rangle = 2.8$ with $\chi^2 = 3.4$. Our result suggests

Table 4
The systematic difference of obtained $\langle \ln A \rangle$ (1σ) for each species by three species analysis

$\log N_e$	P	He	C	Mg	Fe
5.0–5.3 (L)	+0.24	−0.02	±0.00	−0.17	−0.29
5.3–5.6 (L)	+0.21	−0.24	−0.02	−0.23	−0.17
5.5–5.7 (H)	±0.00	−0.29	±0.00	−0.06	±0.00
5.7–5.9 (H)	±0.00	−0.24	±0.00	−0.02	±0.00
5.9–6.1 (H)	±0.00	−0.22	±0.00	−0.08	±0.00
6.1–6.3 (H)	+0.04	−0.12	±0.00	−0.03	±0.00
6.3–6.5 (H)	+0.05	−0.17	±0.00	−0.11	±0.00

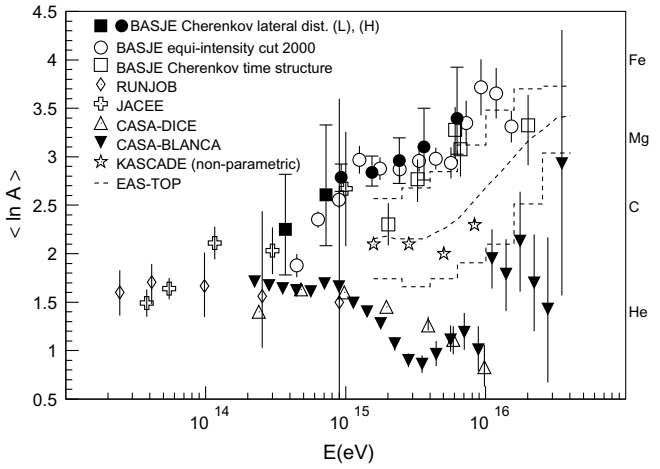

Fig. 15. The present result of the mean logarithmic mass $\langle \ln A \rangle$ compared with the results of other experiments BASJE [1,8], CASA-BLANCA [9], CASA-DICE [10], KASCADE(non-parametric) [11], EAS-TOP [19], and direct measurements (JACEE [6] and RUNJOB [7]).

an increase of heavier component fractions with primary energies of cosmic rays, but the constant composition model cannot be excluded because of the experimental errors. In Fig. 15 we also plot the results of the direct and the indirect measurements. Our present result is consistent with the direct measurement results of JACEE [6] and RUNJOB [7] within the errors at the energies from $10^{14.5}$ to $10^{15.0}$ eV. It must be emphasized that our present result is in agreement with the results of our previous experiments, the measurement of the Čerenkov photon pulse time structures [8] and the equi-intensity method analysis of the EAS size spectra [1]. On the other hand, our results are apparently inconsistent with the results of CASA-BLANCA [9], CASA-DICE [10], KASCADE = nonparametric [11] at the energies around the knee. There are other experiments which did not calculate $\langle \ln A \rangle$ with the primary energy using their results [20–24], and some results in those experiments suggest that the heavy component is enriched at the knee [22–24].

5. Discussion

One of the causes of the systematic uncertainties in the chemical composition is from the hadronic interaction models used in the EAS simulations. In our simulations the parameter β has a model dependence to a certain degree, because this parameter is sensitive to the EAS developments at their early stages. In this work we used the QGSJET model which gives the most rapid development among the major models (SYBILL, QGSJET, DPMJET, and neXus) [25]. Note that the QGSJET model gives more rapid development than that from the newest version QGSJET-II [26]. We found that

$\langle \ln A \rangle$ calculated by using these interaction models are larger than that obtained using the QGSJET model. For example, the $\langle \ln A \rangle$ increases by 0.2 using the SYBILL model compared to that in the case of QGSJET at $\log N_e = 5.5$–5.7. Therefore the present result with QGSJET gives the "lower limit" of $\langle \ln A \rangle$. The other origin of systematic uncertainties in the chemical composition is from the uncertainty in the energy determination using the N_e. The uncertainty in the energy determination, which includes the difference of EAS development and that of fluctuation, depend on species of primary particles and their primary energies. For example, the energy estimations for protons have larger uncertainties than those for heavier nuclei, because the developments of EASs induced by proton have larger fluctuations. Therefore, a part of the protons of lower energies (i.e. of higher intensity) affect the chemical composition at higher energies (i.e. of lower intensity). From this effect, the chemical composition must be estimated lighter than nature systematically. Moreover if the proton energies are overestimated, this systematic effect will be more significant. In this work the effect on the chemical composition is compensated using function (5). The degrees of the effect on $\langle \ln A \rangle$ are less than 0.6 below the energy 10^{15} eV. Above $10^{15.5}$ eV the error caused by this effect become smaller (less than 0.1), because the relations between N_e and primary energies and their fluctuations for different species are almost same above this energy (see Fig. 3). We conclude that the present result below $10^{15.5}$ eV is compensated using function (5) and above this energy is robust for the uncertainties.

For the origins of cosmic rays with energies up to 10^{14} eV, the diffusive shock accelerations in supernova blast waves in the Galaxy are extensively discussed. On the other hand, for cosmic rays of above 10^{14} eV, their origins and acceleration mechanisms are still unknown. At the knee one of the most important problems in cosmic ray studies is whether the cosmic ray origins are of galactic or not. The energy spectrum of the species is continuous and the change in the chemical composition is monotonically below and above the knee [1]. The change can be explained in terms of a rigidity dependence (e.g. [1]) without supposing contributions by extragalactic components.

In addition, it is predicted that the composition of extra-galactic cosmic rays are dominated by protons, because of nuclear spallation in their propagation process and easiness of leakage from their parent galaxy. However, the light components are not dominant at the knee from our results. Therefore, the contribution of extragalactic cosmic rays is considered to be small at the knee.

What kind of objects in the Galaxy do accelerate cosmic rays above 10^{15} eV? Ellison [27] pointed out that in the Galaxy few supernova remnants with a high magnetic field can accelerate nuclei to energies above 10^{15} eV. If most SNRs are incapable of accelerating cosmic rays to such high energies, we need to consider the other acceleration mechanisms and/or sites such as the re-acceleration mechanism at the termination shocks of galactic winds [28] and the shock accelerations with supernova explosions of massive stars with strong stellar winds [3], etc.

The knee in the energy spectrum can be explained in terms of a rigidity dependence (e.g. [1]). From our previous paper [1] the energy spectrum of each of the species shows a bend at the fixed rigidity at $10^{14.5}$ V. It was pointed out that the position of a cutoff in cosmic ray spectrum in terms of rigidity depends on some mechanisms, e.g. a decrease of the acceleration efficiency or an increase of the escape probability from the acceleration site or the Galaxy (e.g. [2]). It is difficult to give a conclusion of the rigidity dependence from our results. To solve this problem we need an experiment such that primary particle type can be identified event-by-event. Above 10^{15} eV, it is possible from a high density measurement of lateral density distributions of atmospheric Čerenkov photons. Event-by-event analysis also needs a small bias for the primary energy estimation. At our altitude, N_e can be useful for that, because of small systematic differences of observed N_e between species, and the same order of fluctuations and determination accuracies (Fig. 3).

6. Conclusions

We have measured the lateral density distributions of atmospheric Čerenkov photons associated with EASs at Mt. Chacaltaya to study the chemical composition of the primary cosmic rays. We have obtained $\langle \ln A \rangle$ in the range from 10^{14} to 10^{16} eV. The present result is consistent with the direct measurement by JACEE and RUNJOB within the experimental errors, and also consistent with the previous BASJE results [1,8]. Our result shows that the values of $\langle \ln A \rangle$ are higher than the logarithmic mass number for carbon and the proton component is no more dominant at the knee.

Acknowledgements

We would like to thank all the staffs of Instituto de Investigaciones Fisicas, Universidad Mayor de San Andres for their daily support to our experiment. We also wish to acknowledge helpful support by the staffs of Institute for Cosmic Ray Research, University of Tokyo. From the Ministry of Education, Culture, Sports, Science and Technology of Japan, this work was supported by a grant-in-aid for Scientific Research, and HT was supported by the 21st Century COE Program at Tokyo Tech "Nanometer-Scale Quantum Physics".

References

[1] S. Ogio et al., Astrophys. J. 612 (2004) 268.
[2] B. Peters, Nuovo Cimento 14 (1961) 436.
[3] P.L. Biermann, Astron. Astrophys. 271 (1993) 649.
[4] A.D. Erlykin, A.W. Wolfendale, J. Phys. G 23 (1997) 979.
[5] K. Kobayakawa et al., Phys. Rev. D 66 (2002) 083004.
[6] Y. Takahashi et al., Nucl. Phys. B (Proc. Suppl.) 60B (1998) 83.
[7] A.V. Apanasenko et al., Astropart. Phys. 16 (2001) 13.
[8] Y. Shirasaki et al., Astropart. Phys. 15 (2001) 357.
[9] J.W. Fowler et al., Astropart. Phys. 15 (2001) 49.
[10] S.P. Swordy, D.B. Kieda, Astropart. Phys. 13 (2000) 137.
[11] T. Antoni et al., Astropart. Phys. 16 (2002) 245.
[12] F. Kakimoto et al., Nucl. Inst. Meth. A373 (1996) 282.
[13] D. Heck et al., Report FZKA 6019, Forschungszentrum Karlsruhe, 1998.
[14] N.N. Kalmykov, S.S. Ostapchenko, Yad. Fiz. 56 (1993) 105.
[15] M. Kobayashi et al., Nucl. Inst. Meth. A337 (1994) 355.
[16] C. Rozsa et al., IEEE NSS, 1999.
[17] J.R. Patterson, A.M. Hillas, J. Phys. G: Nucl. Phys. 9 (1983) 1433.
[18] D. Heck, J. Knapp, Report FZKA 6097, Forschungszentrum Karlsruhe, 1998.
[19] M. Aglietta et al., Astropart. Phys. 20 (2004) 641.
[20] F. Arqueros et al., Astron. Astrophys. 359 (2000) 682.
[21] K. Bernlöhr et al., Astropart. Phys. 8 (1998) 253.
[22] M.A.K. Glasmacher et al., Astropart. Phys. 10 (1999) 291.
[23] J. Huang et al., Astropart. Phys. 18 (2003) 637.
[24] M. Amenomori et al., Phys. Lett. B 632 (2006) 58.
[25] D. Heck, in: Proceedings of the International Cosmic Ray Conference, 2001, p. 233.
[26] S. Ostapchenko, D. Heck, in: Proceedings of the International Cosmic Ray Conference, 2005, p. 135.
[27] D.C. Ellison, Space Sci. Rev. 99 (2001) 305.
[28] J.R. Jokipii, G.E. Morfill, Astrophys. J. 290 (1985) L1.